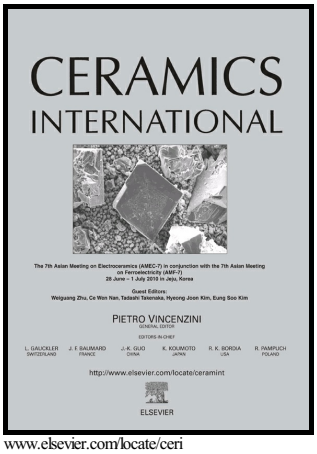

www.elsevier.com/locate/ceri

Composition-dependent $xBa(Zr_{0.2}Ti_{0.8})O_3$-(1-x) $(Ba_{0.7}Ca_{0.3})TiO_3$ bulk ceramics for high energy storage applications

A.R. Jayakrishnan, Kevin V. Alex, Athul Thomas, J.P.B. Silva, K. Kamakshi, Navneet Dabra, K.C. Sekhar, J. Agostinho Moreira, M.J.M. Gomes

PII: S0272-8842(18)33167-5
DOI: https://doi.org/10.1016/j.ceramint.2018.11.250
Reference: CERI20272

To appear in: *Ceramics International*

Received date: 28 September 2018
Revised date: 27 October 2018
Accepted date: 9 November 2018

Cite this article as: A.R. Jayakrishnan, Kevin V. Alex, Athul Thomas, J.P.B. Silva, K. Kamakshi, Navneet Dabra, K.C. Sekhar, J. Agostinho Moreira and M.J.M. Gomes, Composition-dependent $xBa(Zr_{0.2}Ti_{0.8})O_3$-(1-x) $(Ba_{0.7}Ca_{0.3})TiO_3$ bulk ceramics for high energy storage applications, *Ceramics International,* https://doi.org/10.1016/j.ceramint.2018.11.250

Composition-dependent $xBa(Zr_{0.2}Ti_{0.8})O_3$-$(1-x)(Ba_{0.7}Ca_{0.3})TiO_3$ bulk ceramics for high energy storage applications

A R Jayakrishnan[1], Kevin V Alex[1], Athul Thomas[1], J.P.B. Silva[2,3*], K. Kamakshi[4], Navneet Dabra[5], K.C.Sekhar[1*], J. Agostinho Moreira[3], M.J.M Gomes[2]

[1]Department of Physics, School of Basic and Applied Sciences, Central University of Tamil Nadu, Thiruvarur 610 101, India

[2]Centro de Fısica das Universidades do Minho e do Porto (CF-UM-UP), Campus de Gualtar, 4710-057 Braga, Portugal

[3]IFIMUP and IN-Institute of Nanoscience and Nanotechnology, Departamento de Física e Astronomia, Faculdade de Ciências da Universidade do Porto, Rua do Campo Alegre 687, 4169-007 Porto, Portugal

[4]Department of Physics, Madanapalle Institute of Technology & Science, Madanapalle 517325, Andhra Pradesh, India

[5]Mata Sahib Kaur Girls College (affiliated to Punjabi University Patiala), Talwandi Sabo-151302, Punjab, India.

josesilva@fisica.uminho.pt

sekhar.koppole@gmail.com

[*]Corresponding authors.

Abstract

This work reports the composition dependent microstructure, dielectric, ferroelectric and energy storage properties, and the phase transitions sequence of lead free $xBa(Zr_{0.2}Ti_{0.8})O_3$-$(1-x)(Ba_{0.7}Ca_{0.3})TiO_3$ [xBZT-(1-x)BCT] ceramics, with x = 0.4, 0.5 and 0.6, prepared by solid state reaction method. The XRD and Raman scattering results confirm the coexistence of rhombohedral and tetragonal phases at room temperature (RT). The temperature dependence of Raman scattering spectra, dielectric permittivity and polarization points a first phase transition from ferroelectric rhombohedral phase to ferroelectric tetragonal phase at a temperature (T_{R-T}) of 40 ^{0}C and a second phase transition from ferroelectric tetragonal phase - paraelectric pseudocubic phase at a temperature (T_{T-C}) of 110 ^{0}C. The dielectric analysis suggests that the phase transition at T_{T-C} is of diffusive type and the BZT-BCT ceramics are a relaxor type ferroelectric materials. The composition induced variation in the temperature dependence of dielectric losses was correlated with full width half maxima (FWHM) of A_1, E(LO) Raman mode. The saturation polarization (P_s) ≈ 8.3 μC/cm^2 and coercive fields ≈ 2.9 kV/cm were found to be optimum at composition x = 0.6 and is attributed to grain size effect. It is also shown that BZT-BCT ceramics exhibit a fatigue free response up to 10^5 cycles. The effect of a.c. electric field amplitude and temperature on energy storage density and storage efficiency is also discussed. The presence of high T_{T-C} (110 ^{0}C), a high dielectric constant (ε_r ≈ 12285) with low dielectric loss (0.03), good polarization (P_s) ≈ 8.3 μC/cm^2) and large recoverable energy density (W = 121 mJ/cm^3) with an energy storage efficiency (η) of 70 % at an electric field of 25 kV/cm in 0.6BZT-0.4BCT ceramics make them suitable candidates for energy storage capacitor applications.

Keywords: Energy storage capacitors; lead free ceramics; spontaneous polarization; fatigue; dielectric constant; Raman spectroscopy

1. Introduction

Electrical energy storage capacitors are attracting increasing attention due to their potential applications in recoverable energy storage systems owing to their high-power density and fast charge/discharge time compared to that of batteries [1-4]. High dielectric permittivity, low losses and high electric breakdown strength are the major requirements for energy storage capacitors [1-4]. Therefore, the ferroelectric ceramics are always attractive for high energy storage capacitor applications. In this regard, the relaxor doped Lead-zirconate titanate (PZT) ceramics are turned out to be a potential candidates with their impressive energy density (up to 58.1 J/cm^3 at 2805 kV/cm) [5]. Lead based materials have been extensively investigated for energy density applications including thin films. Compared to thin films, bulk ceramics always have advantages due to the low cost of ceramic processing and effective volume to store energy for commercial applications [6-8]. However, due to its toxicity, there is an urgent demand to develop lead free ferroelectric materials for energy storage applications.

On the other hand, $0.5Ba(Zr_{0.2}Ti_{0.8})O_3$-$0.5(Ba_{0.7}Ca_{0.3})TiO_3$ system is considered as most promising lead free electroceramics due to its superior piezoelectric properties ($d_{33}\approx620$ pC/N) comparable with the ones found in lead based materials (PZT) (d_{33} = 500-600pC/N) [9]. This is attributed to the presence of morphotropic phase boundary (MPB) such as the co-existence of the rhombohedral and tetragonal phases that correspond to $Ba(Zr_{0.2}Ti_{0.8})O_3$ (BZT) and $(Ba_{0.7}Ca_{0.3})TiO_3$ **(**BCT) respectively [9]. The MPB region in

x(BZT)-(1-x)BCT ceramics lies in the range of x = 0.15 to 0.6 and is also found to be sensitive to the temperature [10-11]. The BZT-BCT ceramics are further investigated for applications of energy density capacitors [12]. The recoverable energy density was found to be 1.41 J/cm^3 and 0.71 J/cm^3 in BCT and BZT ceramics respectively at 150 kV/cm and 0.94 J/cm^3 in 0.85BZT-0.15BCT at 170 kV/cm [12-13]. The other lead free ferroelectric materials like $0.9Bi_{0.48}La_{0.02}Na_{0.48}Li_{0.02}Ti_{0.98}Zr_{0.02}O_3$-$0.1Na_{0.73}Bi_{0.09}NbO_3$ exhibited an energy storage density of 2.04 J/cm^3 at 178 kV/cm [14].

Most of the investigations for energy density applications have been performed in high electric field region [13-17]. However, the requirement of very high electric field to obtain the high energy density raises several safety concerns. This may constrain its practical applications when it is integrated into portable, wearable and flexible electronic systems which are becoming increasingly important in today's world. Therefore, there is an urgent demand to develop the materials with high dielectric permittivity and low dielectric loss as it can store a large amount of energy even at low electric fields. Further, the materials with high saturation polarization, low remnant polarization and low coercive fields are preferred for energy storage application due to their low hysteresis loss [17]. Thus, recent investigations on energy density capacitors are focused towards the low electric field region. These studies reported that the values of energy densities in $Ba(Ti,Sn)O_3$ and 0.5BZT-0.5BCTceramics are ≈ 30 mJ/cm^3 (at field of 10 kV/cm) and 164 mJ/cm^3 (at 40 kV/cm) respectively[17-18].

In this work, xBZT-(1-x) BCT ceramics with x = 0.4, 0.5, and 0.6, that lie in the MPB region, have been investigated for energy density capacitor applications at low electric fields. The composition change in ceramics promotes relaxor behaviour and thus

enhances the energy storage capacity. Microstructure, dielectric, ferroelectric, energy storage properties and phase transitions studies were systematically investigated. The results demonstrate that the 0.6BZT-0.4BCT ceramics are promising for energy storage application at low electric fields and a wide range of temperature.

2. Materials and Methods

The $xBa(Zr_{0.2}Ti_{0.8})O_3 - (1-x)(Ba_{0.7}Ca_{0.3})TiO_3$ [xBZT-(1-x)BCT] ceramics with x = 0.4,0.5 and 0.6, were prepared by the conventional solid state reaction. The starting raw materials are high purity $BaCO_3$ (99%, Sigma Aldrich), Titanium (IV) oxide (99%, Sigma-Aldrich), $CaCO_3$ (98.5%, Merck – Emplura) and ZrO_2 (97%, Loba Chemie). These reagents were weighted according to the desired stoichiometric ratio, mixed and grinded using a mortar and pestle for 24 hours in pure ethanol. The grinded powder was then calcined in an alumina crucible at a temperature of 1000 ^{0}C for 2 hours in presence of air. We set the time one hour to reach the temperature of 1000 ^{0}C in a muffle furnace. After calcination, the powder was cool down to room temperature naturally. The calcined powder was grinded for one hour and pelletized at a pressure of 5 tons, using KBr Press instrument (Techno search Instruments). The obtained pellets were sintered at 1250 ^{0}C for 3 hrs, and then, pulverized and grinded again for 1 hr. This sintered powder was again pelletized under the previous conditions and further sintered at 1250 ^{0}C for 3 hrs.

The x-ray diffraction (XRD) patterns of double sintered xBZT-(1-x)BCT ceramics were recorded using the Cu K_α radiation (wavelength 0.154 nm), with 0.05^0 step size and a speed of 1^0 per minute (Rigaku, Mini Flex 600). The XRD peaks were deconvoluted using Gaussian distribution function by Origin Software. The unpolarized Raman spectra of BZT-BCT ceramics were obtained in backscattering geometry using an Olympus microscope with a 100x objective. The 514.5 nm line of an Ar^+ laser was used for excitation. The incident power impinging on the sample was kept about 22 mW in order to avoid sample heating. The scattered light was analyzed using a T64000 Jobin-Yvon spectrometer in the 130 - 1000 cm^{-1} spectral range. The spectral resolution was 1 cm^{-1}. For the temperature-dependent Raman scattering measurements, the samples were placed in a THMS600 Linkam Stage. The temperature was measured with an accuracy of 0.1 ^{0}C, after waiting 2 min for temperature stabilization. The Raman scattering spectra were recorded at different fixed temperatures, from room temperature to 150 ^{0}C. The spectra were analyzed by fitting a sum of damped oscillators to the experimental curves as described in ref [19]. The surface morphology of the ceramics was scanned using scanning electron microscope (TESCAN VEGA 3 SBH).

For electrical measurements, a highly conductive silver paste has been coated on the polished surface of pellets [20-28]. The temperature dependence of the dielectric permittivity was measured at different frequencies ranging from 100 Hz to 1 MHz, using Wayne Kerr Impedance Analyzer 6500B in metal-insulator-metal electrode configuration. The P-E hysteresis loops and the fatigue test on the bulk ceramics were recorded using P-E loop tracer (Marine India) by applying an a.c. electric field of amplitudes varying in the range of 10 kV/cm to 35 kV/cm at room temperature. Further,

these characteristics were also studied at different temperatures ranging from RT to 120 ^{0}C with an a.c. electric field amplitude of 25 kV/cm.

3. Results and Discussion

3.1: Crystallographic structure

Fig. 1(a) shows the x-ray diffraction (XRD) patterns of xBZT-(1-x)BCT ceramics, with x = 0.4, 0.5 and 0.6, recorded at room temperature. The crystallographic planes of diffraction peaks were successfully indexed according to the JCPDS file no: 05-0626, 85-0368 [10, 29]. This confirms the formation of BZT-BCT ceramics without any secondary or impurity phases [29]. The extended XRD scans around $2\theta \sim 45.5^0$ are shown in Fig. 1(b) for xBZT-(1-x)BCT ceramics. The peak near $2\theta \sim 45.5^0$ is de-convoluted into two peaks as shown in Fig. 1(c)-(e) and are assigned to of (002) and (200) planes, suggests the existence of the tetragonal (T) phase. Furthermore, the de-convolution peak at $2\theta \sim 66^0$ as shown in Fig. 1(f)-(h) suggests the presence of rhombohedral (R) phase. Therefore, the simultaneous existence of both R and T phases in BZT-BCT ceramics at room temperature confirms its morphotropic phase boundary (MPB) nature and is in good agreement with the literature [9,20]. A lattice parameter refinement program CellCalc [31,32] was used to determine the lattice parameters for both phases based on a least-square method and the results are shown in Table 1. These values here reported are in good agreement with ones reported in the literature [10-11]. The change in lattice parameter with the compositional change could be due to the difference in atomic radii of doping elements as compared to the host element ($R_{Ba} \approx 1.35$ Å; $R_{Ca} \approx 1.00$ Å ; $R_{Zr} \approx 0.72$ Å; $R_{Ti} \approx 0.68$ Å) [20-24]. The tetragonality (c/a) ratio is also shown in Table 1 and is found to be maximum at x = 0.6.

Fig. 2(a)-(c) depicts scanning electron microscope (SEM) images of fractured xBZT-(1-x) BCT ceramics for compositions x = 0.4, 0.5 and 0.6, respectively. SEM images reveal that double sintered BZT-BCT ceramics are dense with a clear contact among the grains with a small porosity. The values of density and relative density are found to be 5.11 g/cm^3, 95%; 5.09 g/cm^3, 93% and 5.03 g/cm^3, 91% for the compositions 0.4, 0.5 and 0.6 respectively. The values observed for x = 0.5 are in agreement with literature [33]. The grain size distribution of BZT-BCT ceramics is shown in Fig. 2(d). The average grain size is found to be 1695 nm, 1065 nm and 430 nm for the compositions x = 0.4, 0.5 and 0.6, respectively. The linear decrease in grain size from x = 0.4 to 0.6 is attributed to the lower grain growth rate that stems from the slow diffusion of Zr^{4+} which has a larger ionic radius than Ti^{4+} [20]. Further, as it can be seen in Fig. 2(d), as x increases, not only the mean grain size decreases but also the grain size distribution width decreases.

3.2 Raman Scattering

3.2.1 Results and Mode Assignment

Fig. 3(a)-(c) shows the unpolarized micro-Raman spectra of xBZT-(1-x) BCT ceramics for compositions x=0.4, 0.5 and 0.6, respectively, recorded at different temperatures, ranging from room temperature to 150 ^{0}C. The Raman spectrum of BZT-BCT ceramics exhibits a similar profile of the one of $BaTiO_3$, as these compounds share the basic unit structure [29-30]. Therefore, modes in BZT-BCT are assigned based on $BaTiO_3$ modes [34-37]. The group theory calculations predict 12 optical vibration modes for the ferroelectric tetragonal phase of $BaTiO_3$: $\Gamma = 3A_1 + B_1 + 4E$ [33]. The A_1 and E modes are both Raman and infrared active, whereas B_1 mode is only Raman active. Due to long-range electrostatic forces associated with lattice ionicity, the A_1 and E optical

phonon modes further split into transverse (TO) and longitudinal optical (LO) modes [35]. Fig. 4 shows a representative example of the fitting result of the Raman spectrum of 0.4BZT-0.6BCT ceramics recorded at room temperature in different spectral ranges. The wavenumber of the Raman-active modes of $BaTiO_3$ and xBZT-(1-x) BCT ceramics, with different compositions, are presented in Table 2. The typical room temperature Raman spectrum of 0.4BZT-0.6BCT ceramics, as shown in Fig. 3(a), consists of a dominant second-order scattering signal which superimposes to six first-order Raman bands, located at around 146 cm^{-1} (marked as peak 1), near 217 cm^{-1} (peak 2), a broad band around 267 cm^{-1} (peak 3), a weak shoulder band at 307 cm^{-1} (peak 4), an asymmetric band near 525 cm^{-1} (peak 5), and a broad weak band at 731 cm^{-1} (peak 6). The existence of the band at ~150 cm^{-1} (1), assigned to the E (TO) mode, clearly evidences for the rhombohedral phase in all BZT-BCT compounds [35]. The peaks 2, 3, 4, 5 and 6 are assigned to A_1 (TO_1), A_1 (TO_2), B_1, E (TO+LO), A_1, E (TO), and A_1, E (LO) phonon modes, respectively [30, 35]. The peaks at 525 cm^{-1} and 731 cm^{-1} correspond to vibrations of the Ba–O bonds, while the band at 307 cm^{-1} corresponds to vibrations of Ti–O bonds [35]. The peaks near 307 cm^{-1} and 731 cm^{-1} confirm the presence of tetragonal symmetry of BZT-BCT ceramics while the peak near 150 cm^{-1} confirms the presence of rhombohedral structure [35]. Therefore, the Raman spectra reveal that all the studied compositions exhibit coexistence of rhombohedral and tetragonal phases at room temperature, corresponding to MPB region.

3.2.2 Composition Dependence of the Raman signal

As the composition varies from 0.4 to 0.6, a shift in the Raman modes can be observed. The frequency of Raman modes can be represented as follows:

$$f = \sqrt{\frac{k}{m}} \quad (1)$$

where *f* is the frequency of the normal mode, k is the force constant, and m is the reduced atomic mass of the elements evolved in the vibration [25]. The modes A_1E (TO) and A_1E (LO) modes related to Ba-O bonds shift towards lower frequency as x increases from 0.4 to 0.6. This is due to a change in reduced mass of the vibrational mode based on the fact that the Ca has lower atomic weight than Ba (m_{Ba}=137.327u; m_{Ca}=40.07u). Similarly, the mode related to Ti-O bond shifts towards lower frequencies due to the higher atomic weight of Zr compared to Ti(m_{Zr}=91.224u; m_{Ti}=47.86u). Since effective mass is linearly proportional to composition, we have plotted $1/f^2$ for the modes versus Ca and Zr content as shown in Fig. 5(a)-(c). For the case of $BaTiO_3$, we use the values that are reported in reference [36]. The linear dependence of $1/f^2$ versus Ca and Zr content suggests that the doping elements are uniformly distributed in the crystal occupying the corresponding sites in the host lattice.

3.2.3 Temperature Dependence

From the fitting results, we have calculated the relative intensity ratio of E(TO) with respect to A_1(TO) mode ($I_{E(TO)}/I_{A1(TO1)}$) and relative intensity ratio of A_1, E (TO) with respect to A_1,E(LO) mode ($I_{A1,E(TO)}/I_{A1,E(LO)}$) and we have followed its temperature dependence. The results are shown in Fig. 6(a)-(b), respectively. The relative intensity ratio ($I_{E(TO)}/I_{A1(TO1)}$) of E(TO) mode related to the rhombohedral phase decreases with increasing temperature and completely vanishes above 40 ^{0}C. Furthermore, relative intensity ratio ($I_{A1,E(TO)}/I_{A1,E(LO)}$) of A_1, E (TO) mode related to the tetragonal structure as shown in Fig. 6(b) increase from room temperature to 50 ^{0}C, and then decreases with the temperature up to 110 ^{0}C and it remains almost constant above 110 ^{0}C. Further, the presence of weak Raman modes above 110 ^{0}C reveals that the tetragonal structure may

not be transformed into ideal cubic Pm3m, due to doping [34]. Usually, doping of different ionic radii elements causes stress, which lower symmetry and activate vibrational modes that are forbidden in the cubic phase [34]. Further, the full width half maxima (FWHM) of the modes A_1, E (LO) around 731 cm^{-1} at different temperatures for different compositions were calculated and shown in Fig. 6(c). One can observe that FWHM is minimum for 0.5 composition up to 80 ^{0}C and sharply rise with further temperature and predominant compared to other compositions.

3.2 Dielectric Properties

Fig. 7(a)-(c) shows the temperature dependence of the dielectric permittivity of xBZT–(1-x)BCT ceramics, measured at different fixed frequencies ranging from 100Hz-1MHz. The values of dielectric permittivity for the compositions x = 0.4, 0.5 and 0.6 are found to be 10720, 12076, 12285 at a frequency of 1 kHz at room temperature, respectively and are shown in Table 3. The values of electric constant here reported are found to be 3-4 times larger than the values reported in the literature [20-24]. The optimum value of dielectric constant at x = 0.6 can be attributed to the small size grain formation as evidenced from SEM analysis. This result is in good agreement with the fact that the dielectric constant of $BaTiO_3$ increases with decreasing the grain size and found to be maximum at a critical grain size. It is shown that the domain wall density increases with decreasing grain size. This could contribute to a maximum in domain wall activity and causes an enhancement in the electric permittivity [38]. Furthermore, maximum dielectric constant in x = 0.6 also correlated to the low frequency vibrational mode of Ba-O bond [39-40].

The temperature dependence of the dielectric permittivity exhibits two anomalies at 40 ^{0}C and 110 ^{0}C for all composition as shown in Fig. 7(a)-(c). By combining Raman and dielectric analysis, the former anomaly is attributed to rhombohedral (ferroelectric) to tetragonal (ferroelectric) phase transformation (T_{R-T} = 40 ^{0}C), while the latter is assigned to tetragonal (ferroelectric) to pseudocubic (paraelectric) phases (T_{T-C}). The values of T_{R-T} and T_{T-C} are in good agreement with the ones reported in the literature [39]. Moreover, as seen in Fig. 7(a)-(c), the phase transition temperature range from tetragonal to pseudocubic is very broad with full width half maxima (FWHM) about 37 ^{0}C, 38 ^{0}C, and 40 ^{0}C for compositions 0.4, 0.5 and 0.6, respectively. The broad curve of dielectric permittivity versus temperature suggests the presence of diffused phase transitions (DPT) in present BZT-BCT ceramics [41-42]. To further quantify the DPT behaviour in the ceramics, the modified Curie–Weiss law proposed by Uchino and Nomura was employed [43]:

$$\frac{1}{\varepsilon_r} - \frac{1}{\varepsilon_m} = \frac{(T - T_m)^\gamma}{C}, 1 \leq \gamma \leq 2, T > T_m \quad (2)$$

where, ε_m the maximum dielectric constant at T_m, while γ and C are constants. The diffuseness exponent 'γ' can vary between 1 (for a normal ferroelectric) to 2 (ideal relaxor ferroelectric). The slope from the plot $\ln(1/\varepsilon_r - 1/\varepsilon_m)$ versus $\ln(T-T_m)$ shown in Fig. 8 gives the diffuseness exponent **γ**. The value of **γ** is found to be in range 1.6 to 1.7 as x increases from x = 0.4 to 0.6 as shown in Table 3. This confirms that our ceramic belongs to a relaxor type ferroelectrics [20]. Further, the degree of diffuseness (δ) parameter for the DPT is obtained from the following relation [41]:

$$C = 2\varepsilon_m \delta^\gamma \quad (3)$$

The y-intercept of the plot $\ln(1/\varepsilon_r - 1/\varepsilon_m)$ versus $\ln(T-T_m)$ shown in Fig. 8 gives the values of C from which, the obtained δ values are 14 ^{0}C, 16 ^{0}C, 24 ^{0}C for x = 0.4, 0.5 and 0.6, respectively. This corroborates that DPT behavior enhances with increasing of BZT content. The origin of DPT behavior in BZT-BCT ceramics might be due to inhomogeneous distribution of Ca and Zr ions in the host Ba and Zr sites and this forms microscopic regions with some degree of microscopic heterogeneity in the composition. The microscopic regions show slightly different Curie temperatures resulting in a diffused phase transition. It is shown that Curie temperatures of different microscopic regions have a Gaussian distribution around some average T_{T-c} [39, 44]. Also, the increase in grain boundary due to a decrease in grain size as evidenced from SEM causes the internal stress and further promote the diffusiveness [20].

Fig. 7(d) shows the plot of dielectric loss versus temperature (tanδ-T) measured at 1 kHz for different compositions. One can notice that for x = 0.5 a different behaviour with temperature compared to the other two compositions is seen. The dielectric losses are minimum up to 80 ^{0}C as compared to 0.4 and 0.6 compositions and increase faster with temperature beyond 80 ^{0}C and become more prominent at high temperature. We noticed a similar trend on the FWHM of the peak A_1E (LO) with temperature as shown in Fig. 6(d). Therefore, the temperature dependence of dielectric losses can be attributed to broadening of the band related to Ba-O mode. It is known that broadening of Raman peak is inversely proportional to the lifetime of phonon vibrations [45-46]. The broad peak corresponds to a shorter lifetime and large phonon interactions. These interactions consume more energy and cause high dielectric losses [45-47].

3.3: Ferroelectric Properties

(a):P-E hysteresis Loop Characteristics

Fig. 9(a)-(c) shows P-E hysteresis loops of x(BZT)-(1-x)BCT, with x = 0.4, 0.5 & 0.6, respectively, recorded at different fixed temperatures in the 27 ^{0}C to 110 ^{0}C range at an a.c. electric field amplitude of 25 kV/cm. The saturation polarization (P_s), and the coercive field (E_c) were estimated for each composition at different temperatures and plotted as a function of temperature as shown in Fig. 10(a)-(b). The room temperature E_c values are found to be 5 kV/cm, 4.9 kV/cm and 2.13 kV/cm for the composition x = 0.4, 0.5 and 0.6, respectively. Such a low coercive field implies that the present BZT-BCT ceramic is "soft" and also upholds the relaxor type behaviour as evidenced from the dielectric analysis [48]. Usually, the relaxor behaviour arises due to the formation of polar nano regions (PNRs). Such PNRs in BZT-BCT arises due to doping of different ionic radii atoms (Ca, Zr) in any of the lattice sites (Ba-site or Ti-site). This can cause distortion in the ABO_3 perovskite structure and results in the formation of local electric field and hinders the long range dipole moment [49]. As shown in Fig. 10(b), the low coercive field for ceramic with x = 0.6 composition than other two compositions at any temperature suggests the enhanced relaxer behaviour and is in good agreement with dielectric analysis. The temperature dependence of P_s and E_c as shown in Fig. 10(a) and (b) also supports the presence of two type transitions as discussed in Raman and dielectric studies. Fig. 9(d) shows the P-E loops for x= 0.6 composition at room temperature under different a.c. electric field amplitudes in the range of 10 to 35 kV/cm. As the field increases, P_r also increases due to the contribution of new domains besides the existing domains.

(b): Fatigue

Since P-E loops gave optimum polarization at the composition x = 0.6, we have performed the fatigue text on 0.6BZT-0.4BCT. Fig. 11(a) shows the saturation polarization as a function of number of switching cycle recorded up to 10^6 cycles at room temperature. One can conclude that the present ceramics are almost fatigue free. The present ceramic shows better fatigue characteristics as compared to the reported values in which P_r is degraded by 1.3% after passing 10^5 cycles [28]. We also studied its fatigue characteristics up to 10^5 cycles at different temperature and are shown in Fig. 11(b). This confirms the stable polarization even at high temperature. Therefore, present ceramics can be useful for applications which are operated over a wide range of temperature.

(c): Energy storage characteristics

The recoverable electrical energy storage density for a relaxor ferroelectric during the charging and discharging process of the capacitor is expressed as [48-49]:

$$W = \int_{P_r}^{P_{max}} E.dP \quad (4)$$

where P_{max} is the maximum polarization and P_r is the remnant polarization. Hence, the energy storage application requires materials with large W together with $\Delta P = (P_{max} - P_r)$.The unrecoverable energy during the discharge process can be considered as energy loss density '$W_{(loss)}$' and can be estimated from the area under the hysteresis loop. The practical energy storage devices not only require high recoverable energy but also demand higher efficiency. The energy storage efficiency for a recoverable energy storage capacitor with an energy loss density is calculated as [48]:

$$\eta = \left(\frac{W}{W+W_{loss}}\right) \times 100 \quad (5)$$

The calculated values of W, $W_{(loss)}$ and the efficiency η of the capacitors with different compositions are tabulated in Table 4. From the table, one can observe that 0.6BZT-0.4BCT shows the optimum efficiency of 70% with a considerable recoverable energy density of 121 mJ/cm^3 at room temperature at an electric field of 25 kV/cm. Fig. 12(a)-(c) shows estimated W values (shaded region in P-E loop) for x =0.6 composition at 30 ^{0}C, 50 ^{0}C and 90 ^{0}C respectively. The variation of W with temperature is shown in Fig. 12(d) which also supports the phases transitions involved in BZT-BCT materials. The effect of a.c. electric field amplitude on energy storage density and efficiency for the composition x = 0.6 was also presented in Table 5. The present BZT-BCT exhibited an energy density of 42 mJ/cm^3 with an efficiency of 62% at 10 kV/cm which is higher than that of values reported in the literature [17]. These studies suggest that 0.6BZT-0.4BCT ceramics are suitable for recoverable energy storage device applications at the low electric field and a wide range of temperature.

Conclusion

This work highlighted the composition and temperature dependence of microstructure, dielectric and ferroelectric properties of xBZT-(1-x)BCT ceramics. The existence of morphotropic phase boundary was confirmed by Raman and dielectric studies. BZT-BCT ceramic undergoes a phase transition from rhombohedral to tetragonal at 40 ^{0}C first and then tetragonal phase was transformed into pseudocubic phase at 110 ^{0}C. The dielectric and ferroelectric analysis further suggested that BZT-BCT ceramic is a relaxor type ferroelectric and this behaviour is found to be increased with an increase of BZT content. Strong correlations have been established between Raman, dielectric and ferroelectric properties. The P-E hysteresis loops exhibited fatigue-free behaviour at

different temperatures. The different parameters like dielectric constant, dielectric loss, polarization, coercive field, the efficiency of energy storage density were found to be optimum for the xBZT-(1-x) BCT ceramics at x =0.6. Therefore, this work suggested that 0.6BZT-0.4BCT ceramics are potential candidates for energy storage capacitor applications.

Acknowledgement

This work was supported by (i) DST-SERB, Govt. of India through grant ECR/2017/000068 and (ii) UGC through Grant Nos. F.4-5(59-FRP/ 2014(BSR)). The authors AR Jayakrishnan acknowledges Central University of Tamil Nadu, India for his Ph.D fellowship**.** K.V.A. acknowledges the DST for the Inspire fellowship IF170601. J.P.B.S. is grateful for the financial support through the FCT Grant SFRH/BPD/92896/2013.The authors thank to Vivek Sudarsanan from the Central University of Kerala for XRD measurements.

References

1. B. Chu et al., A dielectric polymer with high electric energy density and fast discharge speed, Science. 313 (2006) 334–336.

2. S. Tong et al., Lead lanthanum zirconate titanate ceramic thin films for energy storage, ACS Appl. Mater. Interfaces. 5 (2013) 1474–1480.

3. B. Xu, J. Iniguez, and L. Bellaiche, Designing lead-free antiferroelectrics for energy storage, Nature Comm. 8 (2017) 15682.

4. S. Cho et al., Strongly enhanced dielectric and energy storage properties in lead-free perovskite titanate thin films by alloying, Nano Energy. 45 (2018) 398-406.

5. Y. Wang, X. Hao, J. Yang, J. Xu, and D. Zhao, Fabrication and energy-storage performance of (Pb,La)(Zr,Ti)O_3 antiferroelectric thick films derived from polyvinylpyrrolidone modified chemical solution, J. Appl. Phys. 112 (2012) 034105.

6. G. R. Love, Energy storage in ceramic dielectrics, J. Am. Ceram. Soc. 73 (1990) 323-328.

7. X. Hao , J. Zhaia, L. B. Kong, and Z. Xu, A comprehensive review on the progress of lead zirconate-based antiferroelectric materials, Prog Mat.Sci. 63 (2014) 1-57.

8. Y. Zhao, X. Hao, and Q. Zhang, Energy-storage properties and electrocaloric effect of $Pb_{(1-3x/2)}La_xZr_{0.85}Ti_{0.15}O_3$ antiferroelectric thick films, Appl. Mater. Interfaces. 6 (2014) 11633−11639.

9. W. Liu, and X. Ren, Large Piezoelectric Effect in Pb-Free Ceramics, Phys. Rev. Lett. 103 (2009) 257602.

10. S. M. Mane, P. M. Tirmali, and S.B. Kulkarni, Hybrid microwave sintering and shifting of T_c in lead-free ferroelectric composition $x(Ba_{0.7}Ca_{0.3}TiO_3)$-$(1-x)(BaZr_{0.2}Ti_{0.8}O_3)$, Mater. Chem. Phys. 213 (2018) 482–49.

11. S. Sasikumar, R. Saravanan, and S. Saravanakumar, Investigation on charge density, piezoelectric and ferroelectric properties of $(1 - x)Ba(Zr_{0.2}Ti_{0.8})O_3–x(Ba_{0.7}Ca_{0.3})TiO_3$ lead-free piezoceramics, J. Mater. Sci. Mater. Electron. 29 (2018) 1198–1208.

12. V. S. Puli, D. K. Pradhan, B. C. Riggs, D. B. Chriseya, and R. S. Katiyar, Structure, ferroelectric, dielectric and energy storage studies of $Ba_{0.70}Ca_{0.30}TiO_3$, $Ba(Zr_{0.20}Ti_{0.80})O_3$ ceramic capacitors, Inte. Ferroelectrics. 157 (2014) 139–146.

13. V. S. Puli et al., Structure, dielectric, ferroelectric, and energy density properties of $(1 - x)$BZT–xBCT ceramic capacitors for energy storage applications, J. Mater. Sci. 48 (2013) 2151–2157.

14. H. Yang, F. Yan, Y. Lin, T. Wang, and F. Wang, High energy storage density over a broad temperature range in sodium bismuth titanate-based lead-free ceramics, Sci. Rep. 7(2017) 8726.

15. B. Peng et al., Giant electric energy density in epitaxial lead-free thin films with coexistence of ferroelectrics and antiferroelectrics, Adv. Electron. Mater. 1 (2015) 1500052.

16. B. Peng, Z. Xie, Z. Yue, and L. Li, Improvement of the recoverable energy storage density and efficiency by utilizing the linear dielectric response in ferroelectric capacitors, Appl. Phys. Lett. 105 (2014) 052904.

17. J. Gao et al., Enhancing dielectric permittivity for energy-storage devices through tri critical phenomenon, Sci. Rep. 7 (2017) 40916.

18. A. B. Swain, V. Subramanian, and P. Murugavel, The role of precursors on piezoelectric and ferroelectric characteristics of 0.5BCT-0.5BZT ceramic, Ceram. Int. 44 (2018) 6861-6865.

19. J. P. B. Silva et al., Effect of Pt bottom electrode texture selection on the tetragonality and physical properties of $Ba_{0.8}Sr_{0.2}TiO_3$ thin films produced by pulsed laser deposition. J. Appl. Phy. 112 (2012) 044105.

20. Y. Tian, Y. Gong, D. Meng, Y. Li, B. Kuang, Dielectric dispersion, diffuse phase transition, and electrical Properties of BCT–BZT ceramics sintered at a low-temperature, J. Electron. Mater. 44 (2015) 2890–2897.

21. B. Asbani et al., Structural and dielectric properties of a new lead-free ferroelectric $Ba_{0.8}Ca_{0.2}Ti_{0.8}Ge_{0.2}O_3$ ceramics, Superlattices Microstruct. 71 (2014) 162.

22. Z. Yao et al., Titanium deficiency in tetragonal-structured (Ba,Ca)(Zr,Ti)O_3 piezoelectric ceramics, J. Alloys Compd. 712 (2017) 406–411.

23. B. Asbani et al., Lead-free $Ba_{0.8}Ca_{0.2}(Zr_xTi_{1-x})O_3$ ceramics with large electrocaloric effect, Appl. Phys. Lett. 106 (2015) 042902.

24. D. Mezzane et al., Elastic, piezoelectric, and dielectric properties of $Ba(Zr_{0.2}Ti_{0.8})O_3$-50$(Ba_{0.7}Ca_{0.3})TiO_3$ Pb-free ceramic at the morphotropic phase boundary, J. Appl. Phys. 109 (2011) 54110.

25. I. Coondoo, N. J. Panwar, H. Amor, V. E. Ramana, M. Alguer, and A. Kholkin, Enhanced piezoelectric properties of praseodymium-modified

lead-free $(Ba_{0.85}Ca_{0.15})(Ti_{0.90}Zr_{0.10})O_3$ ceramics, J. Am. Ceram. Soc. 98 (2015) 3127–3135.

26. Q. Y. Jiang and L. E. Cross, Effects of porosity on electric fatigue behavior in PLZT and PZT ferroelectric ceramics, J. Mater. Sci. 28 (1993) 4536-4543.

27. H. Weitzing, G. A. Schneider, J. Steffens, M. Hammer, and M. J. Homann, Cyclic fatigue due to electric loading in ferroelectric ceramics, J. Euro. Ceram. Soc. 19 (1999) 1333-1337.

28. Z. Fan, J. Koruza, J. Rödel, and X. Tan, An ideal amplitude window against electric fatigue in $BaTiO_3$-based lead-free piezoelectric materials, Acta. Mater. 151 (2018) 253–259.

29. V. E. Ramana, A. Mahajan, M. P. F. Graça, S. K. Mendiratta, J. M. Monteiro, and M. A. Valente, Structure and ferroelectric studies of $(Ba_{0.85}Ca_{0.15})(Ti_{0.9}Zr_{0.1})O_3$ piezoelectric ceramics, Mater. Res. Bull. 48 (2013) 4395–4401.

30. J. P. B. Silva et al., Ferroelectric phase transitions studies in $0.5Ba(Zr_{0.2}Ti_{0.8})O_3$-$0.5(Ba_{0.7}Ca_{0.3})TiO_3$ ceramics, J. Electroceramics. 35 (2015) 135–140.

31. H. Miura, Cellcalc: A unit cell parameter refinement program on Windows computer, J Cryst Soc Jpn. 45 (2003) 145.

32. M. P. Rao et al, Synthesis of N-doped potassium tantalate perovskite material for environmental applications, J Solid State Chem. 258 (2017) 647-655

33. P. Mishra, Sonia and P. Kumar, Enhanced dielectric and piezoelectric properties of BZT-BCT system near MPB, Ceram. Int. 40 (2014) 14149-14157.

34. X. Deng, X. Wang, H. Wen, A. Kang, Z. Gui, and L. Li, Phase transitions in nanocrystalline barium titanate ceramics prepared by spark plasma sintering, J. Am. Ceram. Soc. 89 (2006) 1059–1064.

35. M. B. Abdessalem, S. Aydi, A. Aydi, N. Abdelmoula, Z. Sassi, and H. Khemakhem, Polymorphic phase transition and morphotropic phase boundary in $Ba_{1-x}Ca_xTi_{1-y}Zr_yO_3$ ceramics, Appl. Phys. A. 123 (2017) 583.

36. T. Noma, S. Wada, M. Yano, and T. Suzuki. Analysis of lattice vibration in fine particles of barium titanate single crystal including the lattice hydroxyl group, J. Appl. Phys. 80 (1996) 5223–5233.

37. V. Buscaglia et al. Grain size and grain boundary-related effects on the properties of nanocrystalline barium titanate ceramics. J. Eur. Ceram. Soc. 26 (2006) 2889–2898.

38. Y. Tan et al., Unfolding grain size effects in barium titanate ferroelectric ceramics. Sci. Rep. 5 (2015) 9953.

39. S. Roy et al., Structural, ferroelectric and piezoelectric properties of chemically processed, low temperature sintered piezoelectric BZT–BCT ceramics, Mater. Res. Express. 3 (2016) 35702

40. Z. X. Chen, Y. Chen, and Y. S. Jiang, DFT study on ferroelectricity of $BaTiO_3$, J. Phys. Chem. B. 105 (2001) 5766–5771.

41. I. Coondoo, N. Panwar, H. Amorín, M. Alguero, and A. L. Kholkin, Synthesis and characterization of lead-free $0.5Ba(Zr_{0.2}Ti_{0.8})O_3$-$0.5(Ba_{0.7}Ca_{0.3})TiO_3$ ceramic, J. Appl. Phys. 113 (2013) 214107.

42. X. G. Tang, K. H. Chew, and H. L. W. Chan, Diffuse phase transition and dielectric tunability of $Ba(Zr_yTi_{1-y})O_3$ relaxor ferroelectric ceramics, Acta Mater. 52 (2004) 5177–5183.

43. R. L. Moreira and R. P. S. M. Lobo, Phenomenological study of diffuse phase transitions. J. Phys. Soc. Japan. 61 (1992) 1992–1995.

44. C. Mao et al., Degraded grain size effect of barium strontium titanate ceramics under a direct current bias electric field, Mater. Res. Express. 4 (2017) 16302.

45. W. C. Hai, et al., XRD and Raman studies on the ordering/disordering of $Ba(Mg_{1/3}Ta_{2/3})O_3$, J. Am. Ceram. Soc. 92 (2009) 1547–1551.

46. M. S. Anwar et al., Structural and optical study of samarium doped cerium oxide thin films prepared by electron beam evaporation, J. Alloys Compd. 509 (2011) 4525–4529.

47. C. T. Chia, Y. Chen, H. F. Cheng, and I. N. Lin, Correlation of microwave dielectric properties and normal vibration modes of $xBa.Mg_{1/3}Ta_{2/3}.O_3$–(1-x)$Ba.Mg_{1/3}Nb_{2/3}.O_3$ ceramics, J. Appl. Phys. 94 (2003) 3360.

48. F. Benabdallah, A. Simon, H. Khemakhem, C. Elissalde, and M. Maglione, Linking large piezoelectric coefficients to highly flexible polarization of lead free $BaTiO_3$-$CaTiO_3$-$BaZrO_3$ ceramics, J. Appl. Phys. 109 (2011) 124116.

49. B. Qu, H. Du, and Z. Yang, Lead free relaxor ferroelectric ceramics with high optical transparency and energy storage ability, J. Mater. Chem. C. 4 (2016) 1795-1803.

Fig. 1: (a) XRD pattern of xBZT-(1-x) BCT ceramics with x = 0.4-0.6 (dotted lines corresponds to JCPDS data). (b) shows the extended XRD scan around $2\theta = 45.5^0$.(c)-(e) shows de-convolution of peak at $2\theta = 45.5^0$ and (f-h) de-convolution of peak at $2\theta = 45.5^0$ at $2\theta = 66^0$ for x =0.4, 0.5 and 0.6 respectively.

Fig. 2: (a-c): SEM images of fractured xBZT-(1-x)BCT ceramics for composition x = 0.4, 0.5 and 0.6 respectively and; (d) grain size distribution.

Fig. 3: (a)-(c) corresponds to Raman spectra of xBZT-(1-x) BCT ceramics for the composition x = 0.4; 0.5; and 0.6 respectively at different temperatures.

Fig. 4: Shows the fitting result of the Raman spectrum of 0.4BZT-0.6BCT ceramics recorded at room temperature in different spectral ranges.

Fig. 5: Frequency^{-2} ($1/f^2$) variation of (a) B_1,E(TO+LO) mode with Zr content, (b) A_1,E(TO) mode with Ca content and (c) A_1,E(LO) mode with Ca content.

Fig. 6: (a): Plot of $I_{E(TO)}/ I_{A1(TO1)}$ ratio versus temperature (b): Plot of $I_{A1,E(TO)}/ I_{A1,E(LO)}$ ratio versus temperature and (c) FWHM of A_1,E(LO) mode versus temperature in xBZT-(1-x)BCT ceramics with x = 0.4, 0.5, 0.6.

Fig. 7: Temperature dependent variation of dielectric constant (ε_r):(a) x=0.4, (b) x=0.5, (c) x=0.6 at various frequencies and (d) the dielectric loss($\tan\delta$) at 1kHz frequency for xBZT-(1-x)BCT ceramics.

Fig. 8: Plot of log $(1/\varepsilon_r - 1/\varepsilon_m)$ versus log $(T-T_m)$ for the composition x= 0.4, 0.5, 0.6 respectively.

Fig. 9: Temperature dependent P-E loop of xBZT-(1-x)BCT ceramic with (a) x=0.4, (b) x=0.5, (c) x=0.6 and ;(d) P-E loop of 0.6BZT-0.4BCT at different amplitudes of electric field.

Figure 10: Temperature dependence of (a) saturation polarization(P_s) and (b)coercive field(E_c) xBZT-(1-x)BCT ceramics for different compositions.

Fig. 11: (a) plot of saturation polarization (P_s) versus number of cycles up to 10^6 at room temperature and (b) Plot of Ps versus number of cycles up to 10^5 at different temperatures.

Fig. 12: Estimation of recoverable energy density for x=0.6 composition at (a) 30 ^{0}C; (b) 50 ^{0}C; (c) 90 ^{0}C and (d) plot of recoverable energy density as a function of temperature.

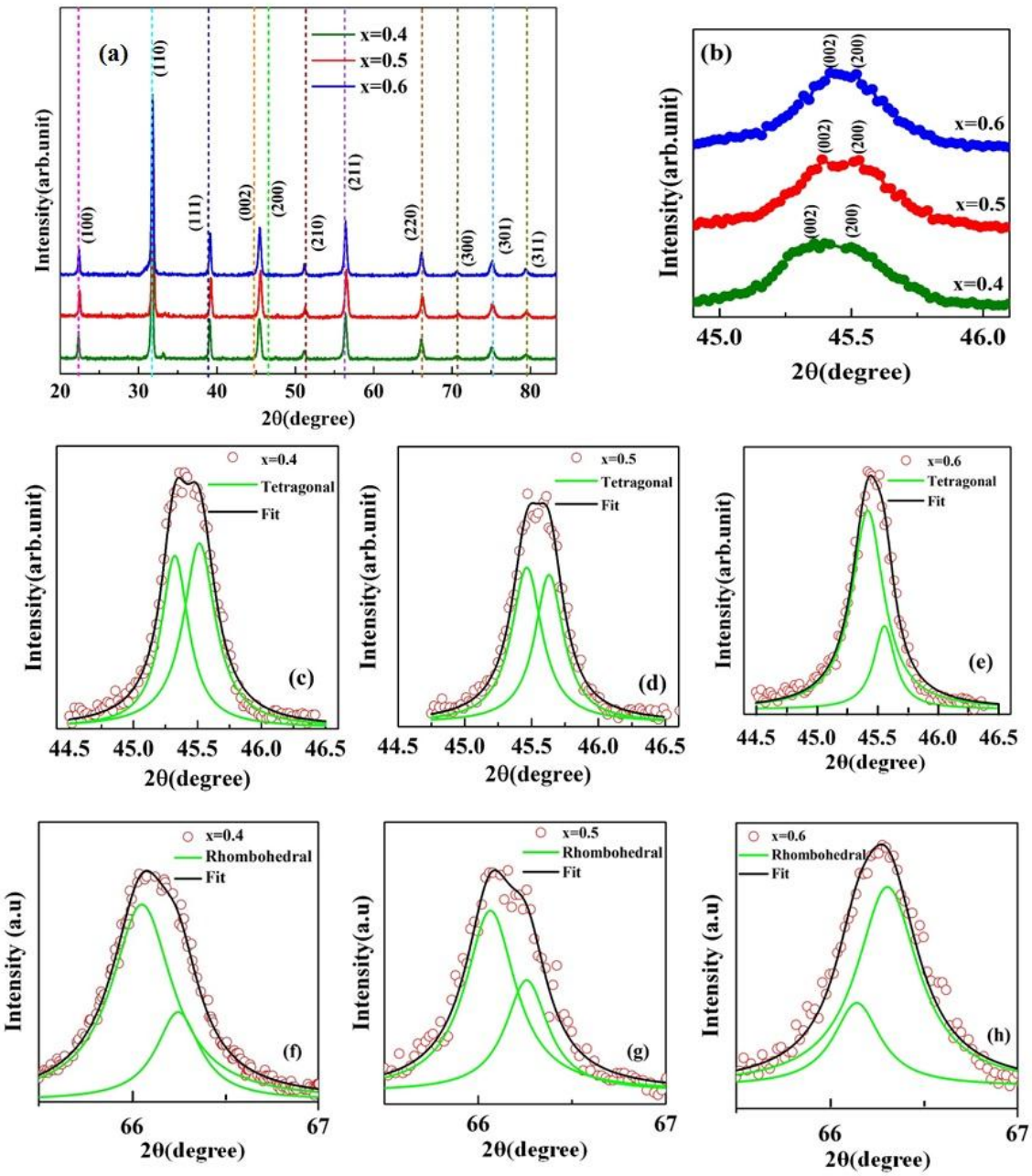
(a)
x=0.4
x=0.5
x=0.6
(100)
(110)
(111)
(002)
(200)
(210)
(211)
(220)
(300)
(301)
(311)
Intensity(arb.unit)
2θ(degree)
(b)
(002)
(200)
x=0.6
x=0.5
x=0.4
Intensity(arb.unit)
2θ(degree)
x=0.4
Tetragonal
Fit
(c)
x=0.5
(d)
x=0.6
(e)
Intensity(arb.unit)
2θ(degree)
x=0.4
Rhombohedral
Fit
(f)
x=0.5
(g)
x=0.6
(h)
Intensity (a.u)
Intensity(a.u)
2θ(degree)

Fig. 1

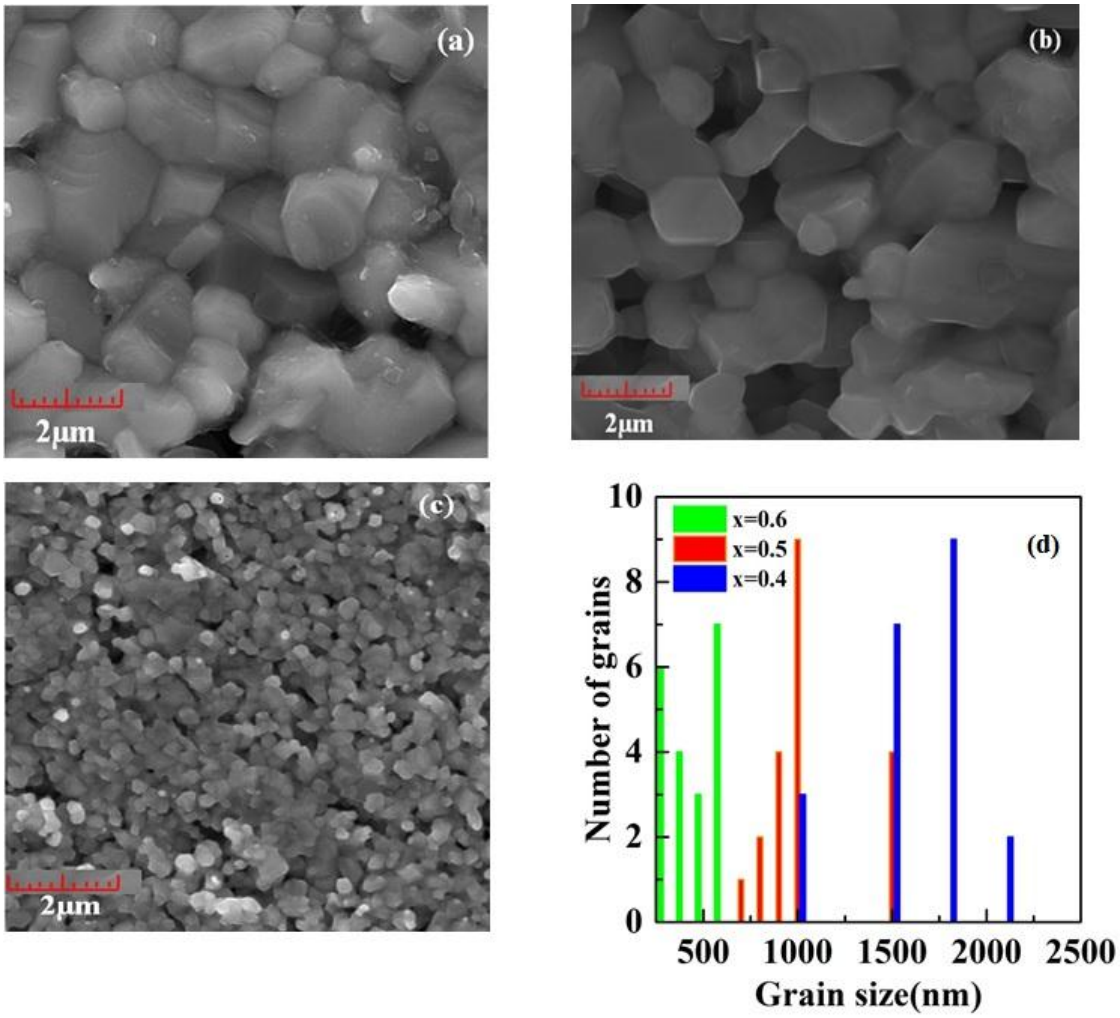

Fig. 2

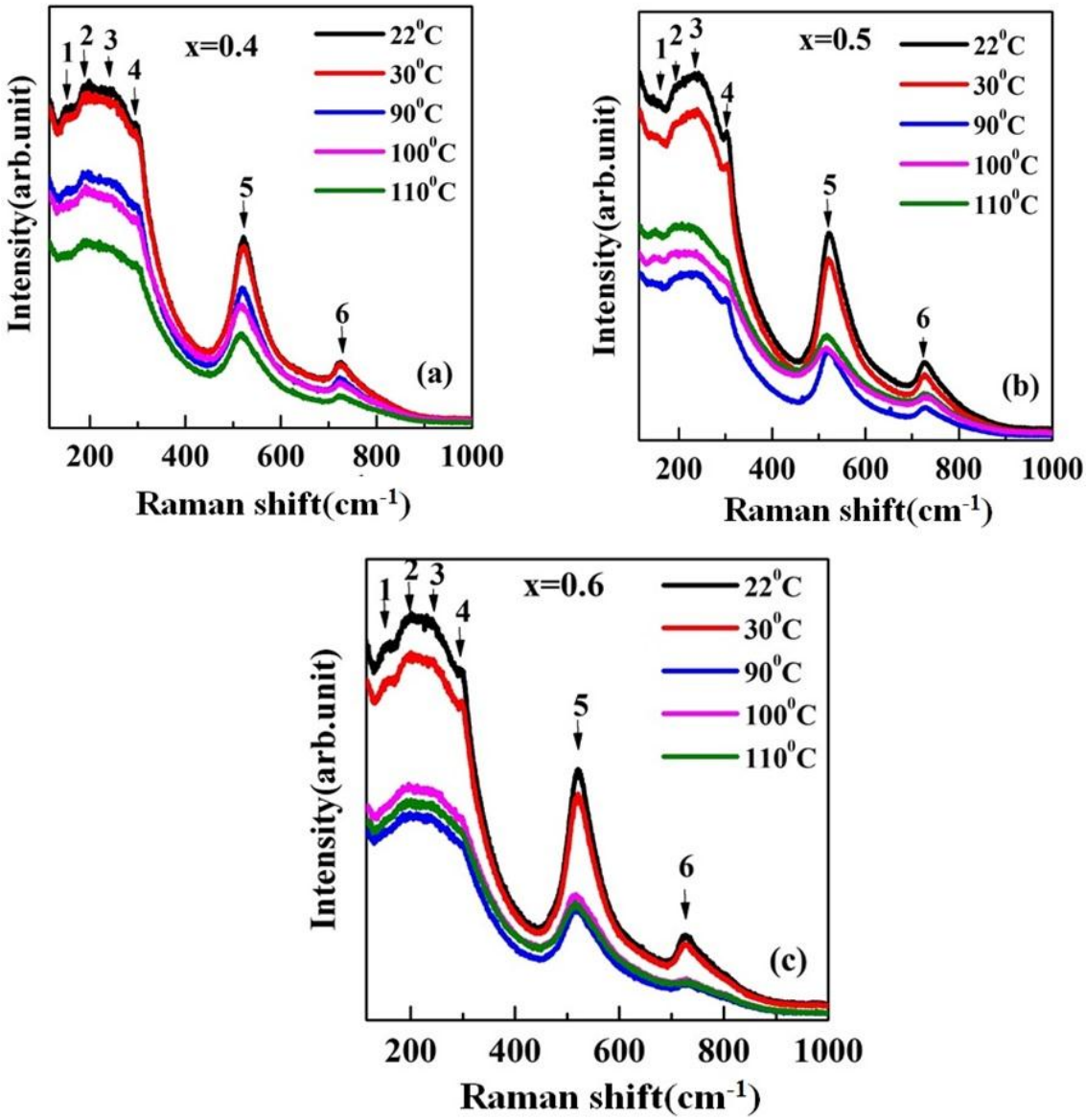
x=0.4
x=0.5
x=0.6
22°C
30°C
90°C
100°C
110°C
1
2
3
4
5
6
(a)
(b)
(c)
Intensity(arb.unit)
Raman shift(cm-1)
200
400
600
800
1000

Fig. 3

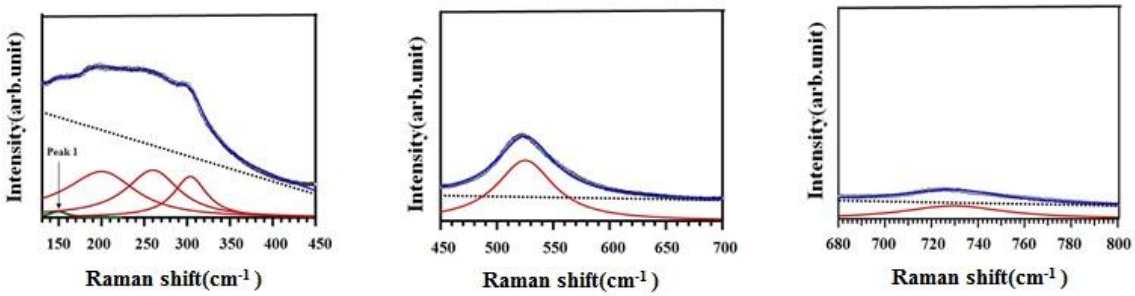
Intensity(arb.unit)
Peak 1
Raman shift(cm-1)
150
200
250
300
350
400
450
450
500
550
600
650
700
680
700
720
740
760
780
800

Fig. 4

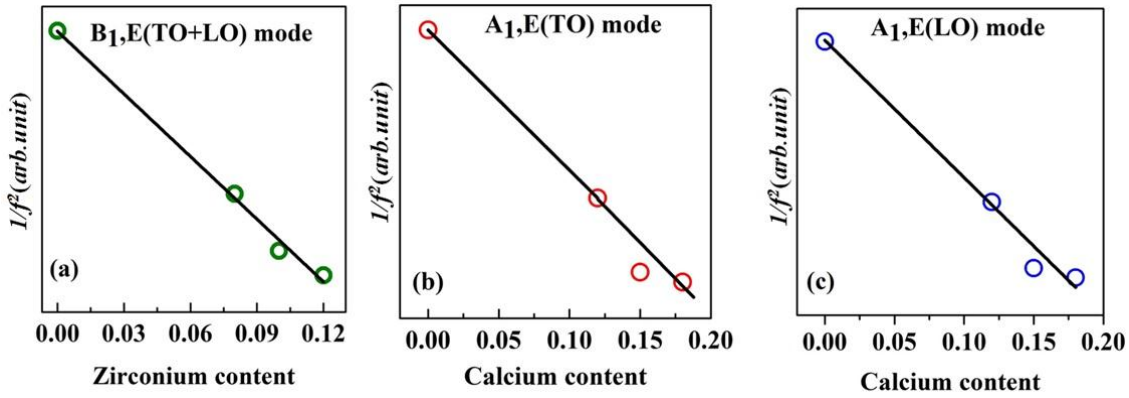
B1,E(TO+LO) mode
A1,E(TO) mode
A1,E(LO) mode
1/f²(arb.unit)
(a)
(b)
(c)
0.00 0.03 0.06 0.09 0.12
Zirconium content
0.00 0.05 0.10 0.15 0.20
Calcium content
0.00 0.05 0.10 0.15 0.20
Calcium content

Fig. 5

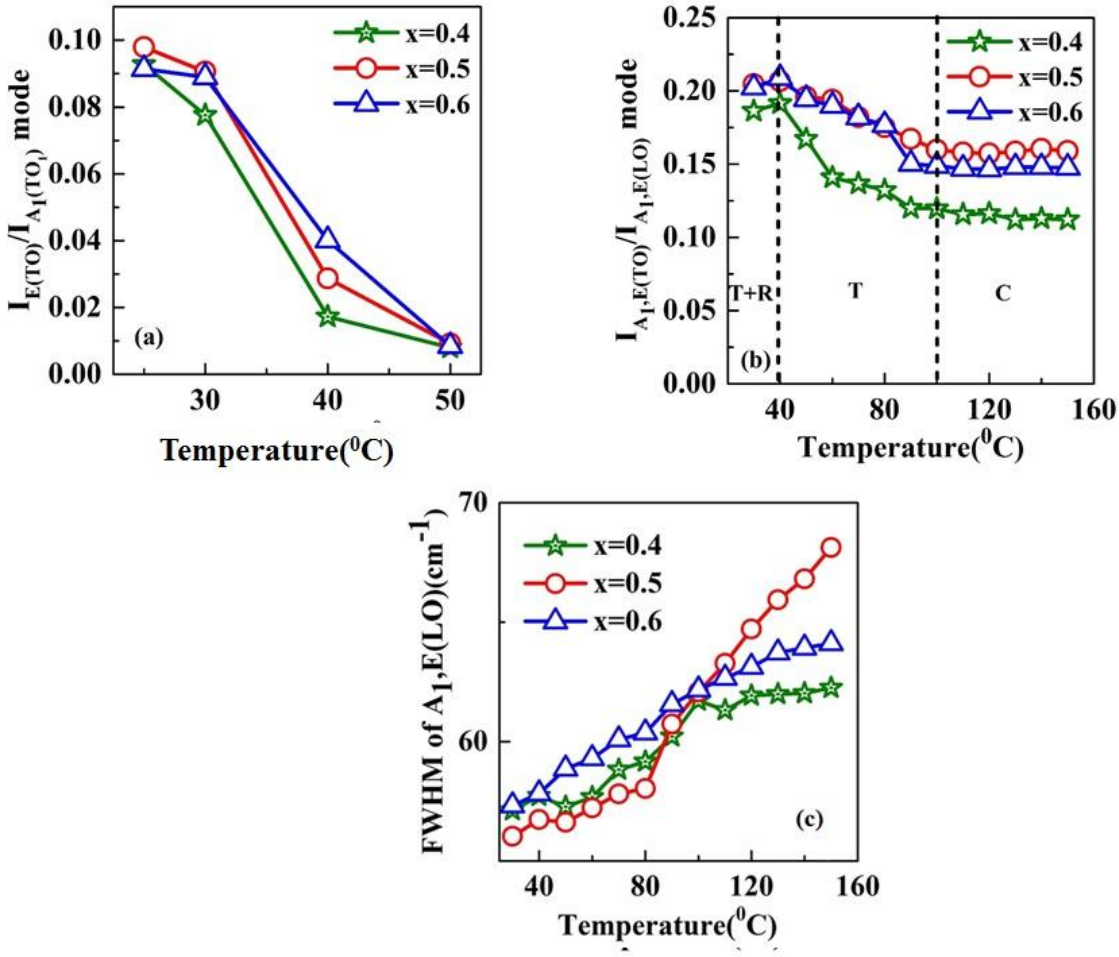
x=0.4
x=0.5
x=0.6
(a)
Temperature(⁰C)
(b)
T+R
T
C
Temperature(⁰C)
FWHM of A1,E(LO)(cm⁻¹)
(c)
Temperature(⁰C)

Fig. 6

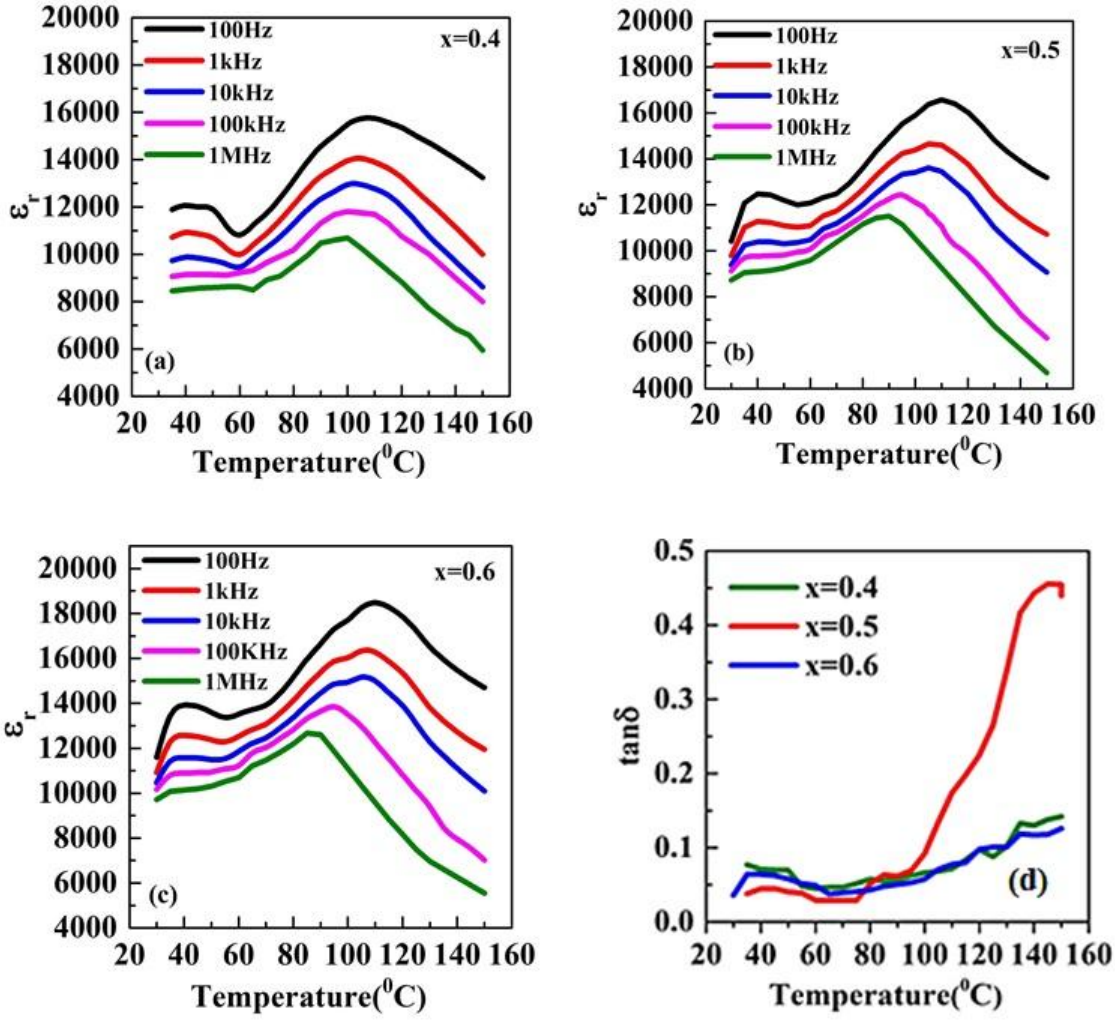

Fig. 7

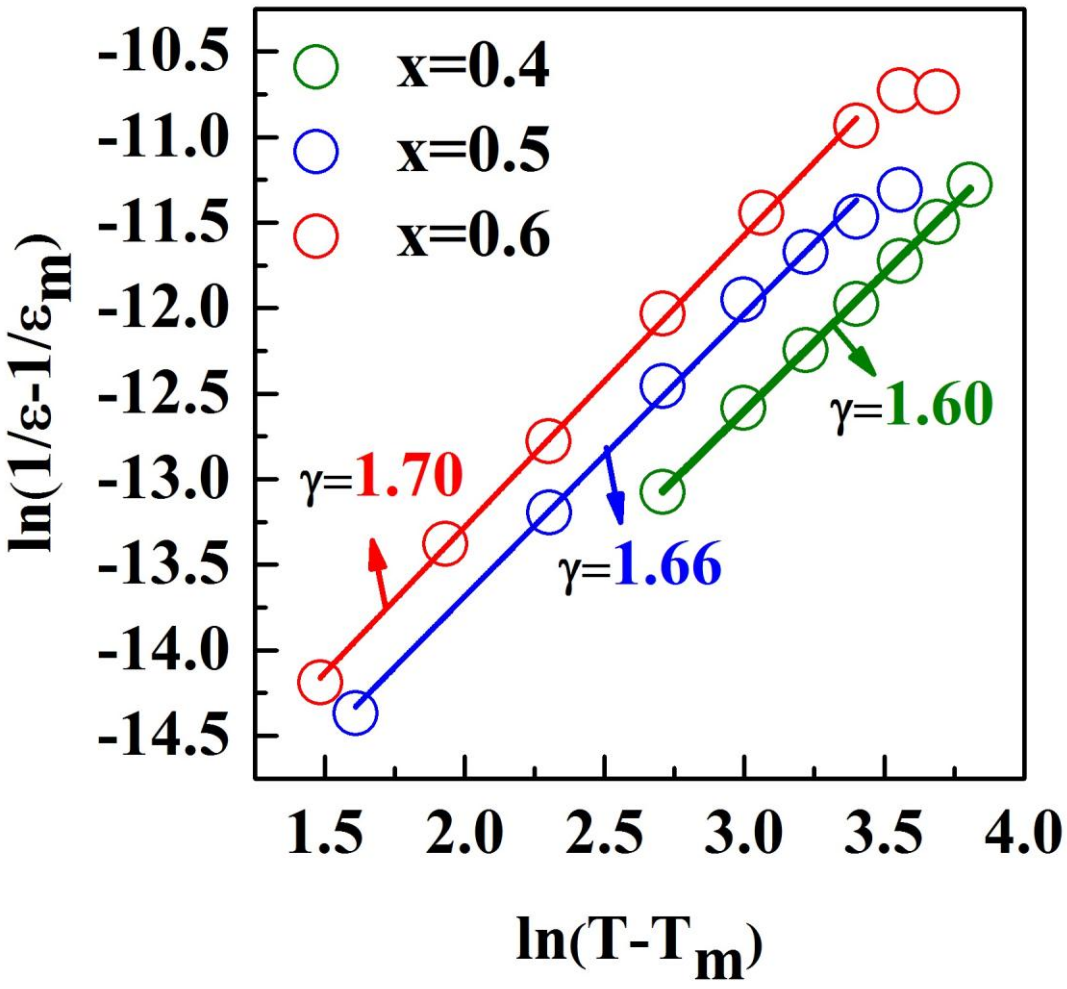

Fig. 8

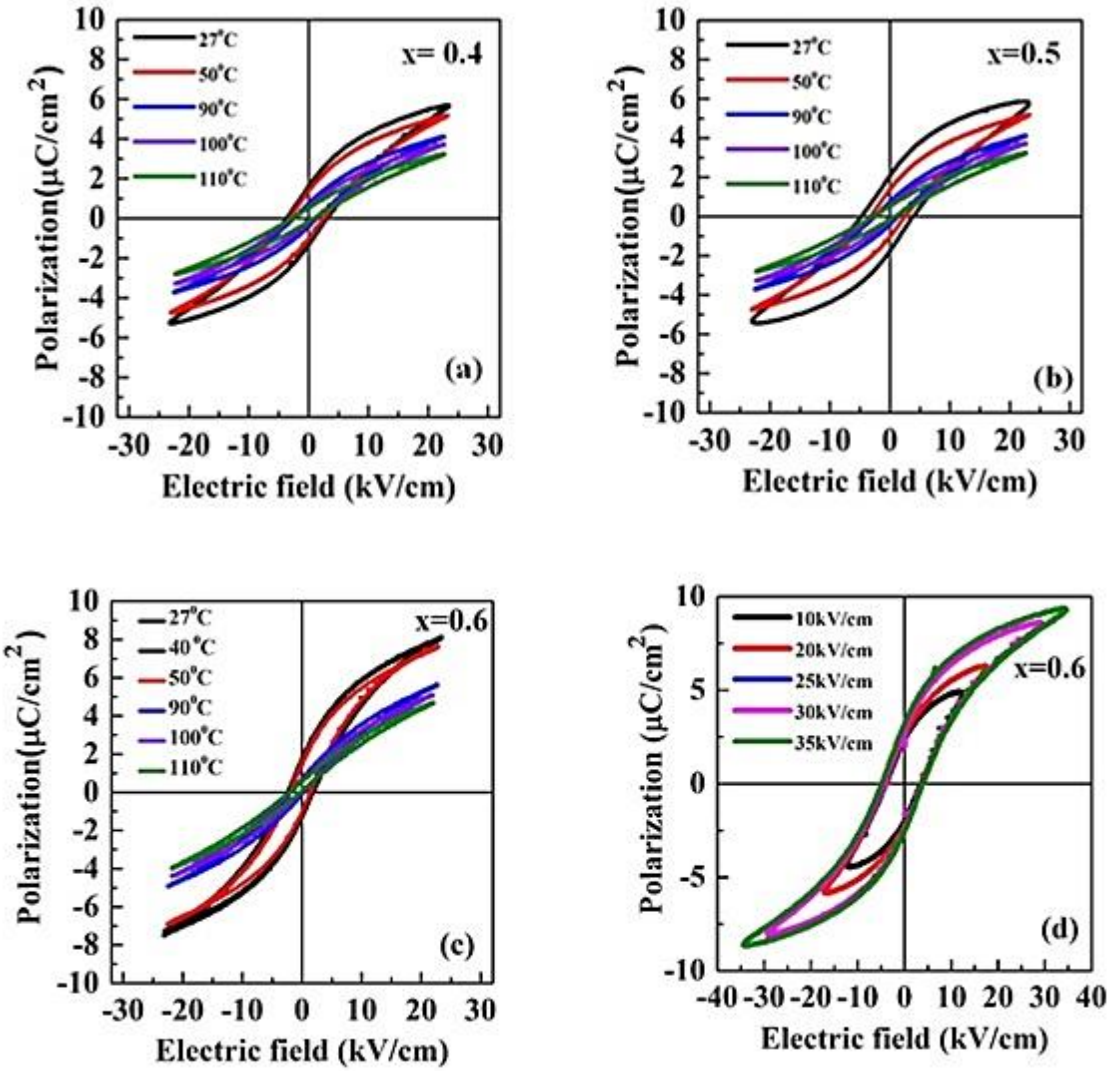

Fig. 9

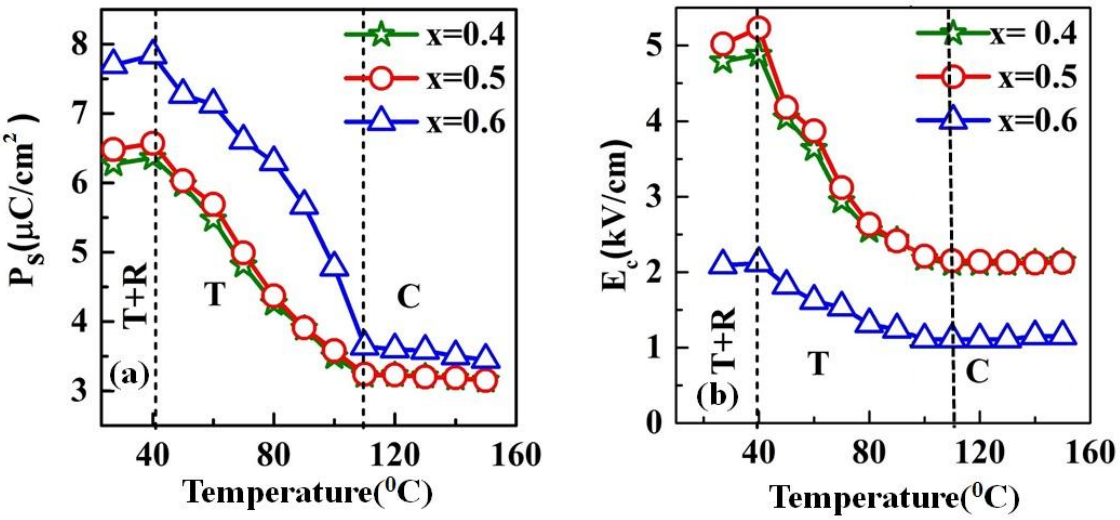
x=0.4
x=0.5
x=0.6
$P_S(\mu C/cm^2)$
T+R
T
C
(a)
Temperature(^{0}C)
E_c(kV/cm)
(b)

Fig. 10

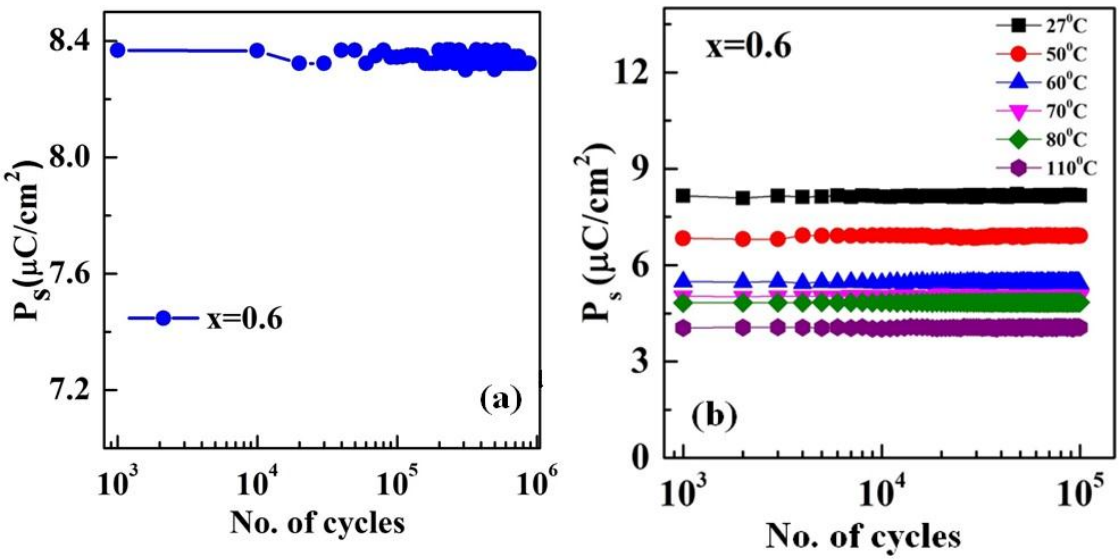
x=0.6
$P_S(\mu C/cm^2)$
(a)
No. of cycles
27^{0}C
50^{0}C
60^{0}C
70^{0}C
80^{0}C
110^{0}C
P_s (μC/cm^2)
(b)

Fig. 11

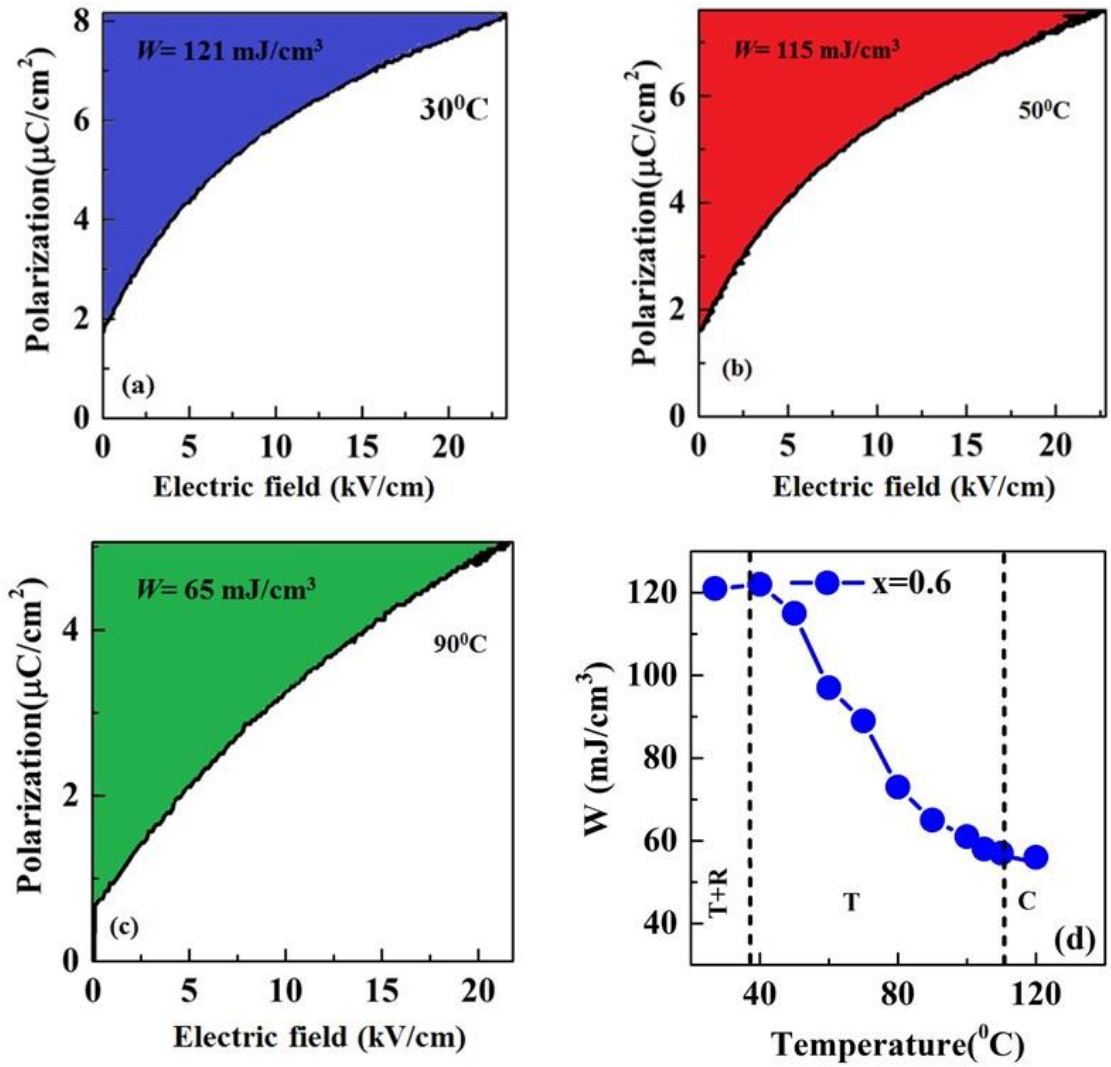

Fig. 12

Table 1: Effect of composition on lattice parameters for both tetragonal and rhombohedral phase in xBZT-(1-x) BCT ceramics.

	Tetragonal Phase				Rhombohedral Phase			
Composition (x)	**a=b (Å)**	**c (Å)**	**c/a ratio**	**Volume $(Å)^3$**	**a (Å)**	**(α^0)**	**Volume $(Å)^3$**	**Crystallite size(nm)**
0.4	3.9965±0.0003	3.9998±0.0006	1.0005	63.88	4.0092±0.0008	89.09	63.86	35
0.5	3.9959±0.0002	4.0027±0.0006	1.0012	63.91	4.0114±0.0005	89.13	63.97	31
0.6	3.9947±0.0002	4.0062±0.0002	1.0029	63.93	4.0144±0.0003	89.22	64.12	25

Table 2: Assignment of Raman modes in $BaTiO_3$ and xBZT-(1-x) BCT ceramics at room temperature.

Sl no.	Mode assigned	Structure	Raman shift(cm^{-1})				Reference
			$BaTiO_3$	**x=0.4**	**x=0.5**	**x=0.6**	
1	E(TO)	R	166	146	149	151	[34-35]
2	$A_1(TO_1)$	R	185	217	215	212	[34-35]
3	$A_1(TO_2)$	R	260	267	264	261	[34-35]
4	B_1,E(TO+LO)	T	298	304	301	300	[30, 34-35]
5	$A_1(TO_3)$	T	515	525	524	523	[30, 34-35]
6	A_1, E(LO)	T	720	731	730	729	[30, 34-35]

Table 3: Composition dependent phase transition temperature (T_{T-C}), dielectric permittivity (1kHz) at room temperature (RT) and at T_{T-C}; diffusivity factor (γ), and degree of diffuseness (δ).

Composition (x)	**T_{T-C} (^{0}C)**	**ε_r (at RT)**	**ε_r (at T_{T-C})**	**γ**	**δ**
0.4	110	10720	14195	1.60	14
0.5	110	11025	14641	1.66	16
0.6	110	12285	16420	1.70	24

Table 4: Composition dependent recoverable energy storage density (W), energy loss density (W_{loss}) and energy storage efficiency (η %) in xBZT-(1-x)BCT ceramics.

Composition (x)	**W (mJ/cm^3)**	**W_{loss} (mJ/cm^3)**	**η (%)**
0.4	85	56	60
0.5	78	56	58
0.6	121	52	70

Table 5: Electric field amplitude dependent recoverable energy storage density (W), energy loss density (W_{loss}) and energy storage efficiency (η %) for x=0.6 composition.

Electric field (kV/cm)	**W (mJ/cm^3)**	**W_{loss} (mJ/cm^3)**	**η (%)**
10	42	25	62
15	65	36	64
20	82	44	65
25	121	52	70
30	132	53	71
35	149	57	72